RESEARCH ARTICLE | MAY 06 2026

Unimolecular decomposition of formic acid cation ($HCOOH^+$): Theory and experiment

A. Gloriod; A. R. Milosavljević ; A. Bellili ; J. Palaudoux; F. Penent ; R. Dupuy ; M. Hochlaf

J. Chem. Phys. 164, 174313 (2026)
https://doi.org/10.1063/5.0325779

The Journal of Chemical Physics ARTICLE pubs.aip.org/aip/jcp

Unimolecular decomposition of formic acid cation ($HCOOH^+$): Theory and experiment

Cite as: J. Chem. Phys. 164, 174313 (2026); doi: 10.1063/5.0325779
Submitted: 2 February 2026 • Accepted: 13 April 2026 •
Published Online: 6 May 2026

A. Gloriod,[1] A. R. Milosavljević,[2,a)] A. Bellili,[3] J. Palaudoux,[4] F. Penent,[4] R. Dupuy,[4] and M. Hochlaf[1,a)]

AFFILIATIONS

[1] Université Gustave Eiffel, COSYS/IMSE, 5 Bd Descartes, 77454 Champs sur Marne, France
[2] Synchrotron SOLEIL, Saint-Aubin, BP 48, F-91192 Gif-sur-Yvette Cedex, France
[3] Faculty of Chemistry, USTHB, Laboratory of Thermodynamics and Molecular Modeling, BP32, El Alia, Bab Ezzouar, 16111 Algiers, Algeria
[4] Sorbonne Université, CNRS, Laboratoire de Chimie Physique–Matière et Rayonnement, LCPMR, 75005 Paris, France

[a)] **Authors to whom correspondence should be addressed:** aleksandar.milosavljevic@synchrotron-soleil.fr and majdi.hochlaf@univ-eiffel.fr

ABSTRACT

The unimolecular decomposition of formic acid, FA, upon single-photon ionization is investigated by means of synchrotron radiation coupled to a photoelectron/Auger electron–photoion coincidence setup, allowing to identify the ionic products coming from state-to-state fragmentation upon ionization. We show that the C–O bond breaking and the proton ejection from ionized FA are the major processes, whereas H_2O^+ formation is a minor channel. For interpretation, we performed theoretical computations using post-Hartree–Fock *ab initio* computations to determine the neutral and ionic species formed during these experiments and the corresponding dissociation channels. We also mapped the potential energy surfaces of FA^+ of doublet and quartet electronic states and its isomers along the reactive coordinates. Computations reveal that the major products are HCO^+ or COH^+ and $HOCO^+$ or HCO_2^+ isomeric forms, depending on the initially populated parent cationic electronic state. Dissociation proceeds either directly or after intramolecular isomerization processes, via the $HOCOH^+$ or H_2OCO^+ isomers. We also highlighted the importance of vibronic and spin–orbit couplings during these processes.

I. INTRODUCTION

Formic acid, HCOOH (FA), is the simplest and most abundant carboxylic acid in the atmosphere. It is emitted from both natural and anthropogenic sources and plays a significant role in the acidification of rain. The photophysics, (photo)chemistry, and reactivity of FA are very rich and complex and take place across the gas phase, liquid and solid aerosols, and at interfaces. It is connected to the reactivity of Criegee intermediates and of HOCO, as well as the conversion of CO into CO_2.[1] In particular, the UV photolysis of FA represents the main degradation channel in the stratosphere.[2] Dissociation proceeds dominantly through the non-obvious CO + H_2O and H_2 + CO_2 products at low excitation energies, whereas the simple bond-breaking products (i.e., H + COOH/HCOO and HCO + OH) may be obtained at higher energies (see Refs. 3–5 for more details).

FA is also of astrophysical relevance, being the first carboxylic acid to be detected in the interstellar medium (ISM). Indeed, Zuckerman *et al.*[6] in 1971 used radioastronomy to identify the *trans* form of this acid (Scheme 1) in the stellar cloud Sagittarius B220 as confirmed in 1975 by Winnewisser and Churchwell.[7] Since then, *trans*-FA has been definitely detected in several astrophysical objects. More recently, the less stable form of FA, i.e., *cis*-FA (Scheme 1), was also detected.[8–10] By contrast, none of the conformers of the FA cation, $HCOOH^+$, have yet been detected in astrophysical media, although some of its fragments were already identified. In fact, the astrophysical media in which its neutral form was found are irradiated by ionizing light, which could lead to the formation of FA^+ and its fragments. For instance, $HOCO^+$, that could be obtained after hydrogen loss from FA^+, is known to be present in the ISM since the beginning of the 1980s.[11,12] The HCO^+ cation, which can be formed by C–O bond breaking of FA^+, was also detected in the ISM

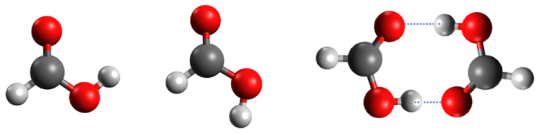

SCHEME 1. Molecular structures of *trans*-HCOOH (*trans*-FA), *cis*-HCOOH (*cis*-FA), and $(HCOOH)_2$ dimer.

in the early 1970s.[13,14] Both ions are participating in the rich ionic chemistry taking place in dense clouds, as pointed out by Herbst and Klemperer.[15] To explain the non-detection of FA^+ in gas-phase ISM, Boechat-Roberty *et al.*[16] proposed the efficient destruction of FA, just evaporating from the interstellar grains, by soft X-rays, abundant in PDR regions, since the photodissociation cross section of FA is quite large.

Knowledge of the stability of molecular species against ionizing light and their further unimolecular decomposition processes are mandatory for confirming their presence and for estimating their abundances and the subsequent possible detection in astrophysical media. This motivated several works dealing with the interaction of vacuum ultraviolet (VUV) light with FA. Previous photoelectron spectroscopic studies determined the (adiabatic) ionization energy of FA at ~11.30 eV.[17–20] These works showed that these spectra are composed of five bands in the 11–19 eV energy range, where the first, the second, and the fifth ones present vibrational structures, whereas the third and the fourth bands are congested due to vibronic couplings and predissociation-induced processes involving the electronic states of FA^+.[21]

In 1980, Niwa *et al.*[22] investigated the dissociative photoionization of FA using photoelectron-photoion coincidence (PEPICO) spectroscopy. They observed the formation of the HCO^+ fragment in state-specific, rather than statistical, dissociations. This is confirmed in 1989 by the TPEPICO study of Nishimura *et al.*[23] via the analysis of the kinetic energy releases (KERs) of the HCO^+ fragment in the 11–19 eV energy range. In 2002, Leach and coworkers'[24,25] investigated the photoabsorption, photodissociation, and fragment fluorescence of FA in the 6–23 eV range. For $h\nu < 13.6$ eV, mostly neutral fragmentations are observed, producing OH + HCO and CO_2 + 2H. Above 13.6 eV, the FA^+ cation dissociation dominates, producing mainly $COOH^+$ + H and HCO^+/COH^+ + OH. It is also worth noting that a strong autoionization was observed in the 15.7–16.8 eV energy domain, complicating even more the dynamics of FA-induced VUV processes in that energy range. In 2005, Tepnual *et al.*[26] detected $HCOO^+$ and CHO^+ ions signal while colliding energetic FA^+ ions with a hydrocarbon stainless steel surface because of CH and CO bond breakings. One year later, Pilling *et al.*[27] carried out ionization and dissociation of FA by employing fast electrons (0.5–2 keV) and energetic protons (0.128–2 MeV) as projectiles, simulating solar-wind-induced effects. Their TOF mass spectrum is dominated by a peak corresponding to CO^+ ion in addition to some smaller peaks of FA^+, O_2^+, CO_2^+, H_2O^+, O^+, and CH^+ ions, quite different from those obtained by Leach and workers. In 2012, Siggel-King *et al.*[28] and Arruda *et al.*[29] recorded the total and partial ion yield of gaseous FA in the valence region (11–20 eV range). They pointed out the formation of the H_2O^+ ionic fragment in addition to the already known FA^+, $COOH^+$, and HCO^+ ions. The formation of H_2O^+ was confirmed by Fujimoto *et al.*[30] in 2020. Concerning the core ionization of FA, earlier work by Boechat-Roberty *et al.*[16] in the 200–310 eV range showed that the intermediate FA^+ ions fragment to produce CO^+ (with a good yield of ~36%), and CH_2^+, O^+, HCO^+/COH^+, and O_2^+ ions to a lesser extent. More recently, Stråhlman *et al.*[31] measured mainly positive and negative atomic ions after fragmentation of core-excited FA molecules. Note that multiphoton-induced fragmentation–ionization of FA leads to the formation of 12 ionic species including H^+, C^+, and OH^+, COH_2^+ in addition to those discussed above.[32] From a theoretical point of view, the ground-state potential of FA^+ was mapped at the SD-CI/6-31G**//UHF/4-31G[33] and MP3/6-31G*//HF4-31G[34] relatively low levels of theory to characterize the isomeric forms of this cation, the transition states connecting these isomers, and its lowest dissociation limits. Nevertheless, there were no investigations of the involvement of the electronic states of these species in the unimolecular decomposition of FA^+.

The fragmentation dynamics of the electronic states of FA^+ is non-statistical and is quite different from that of the corresponding neutral. The outcomes of this fragmentation depend on the excitation scheme (single photon, multiphoton, electrons, . . .). Nevertheless, a close screening of the literature shows that there are no studies of the state-to-state unimolecular decay of FA^+ prepared by single-photon ionizing FA. In other terms, there were no electron-energy-resolved studies of the fragmentation of different electronic states separately. Also, there are no theoretical investigations of the state-to-state reaction pathways undertaken by FA^+ ions, in its electronic ground state and/or in its electronically excited states, reaching the respective dissociation channels. In particular, there is no clear evidence of the unique existence of *cis*-FA, *trans*-FA, or $(HCOOH)_2$ dimer species, or a mixture of them in the experiments prior to ionization. In addition, the role of the vibronic couplings and predissociation[21] in the unimolecular decomposition of FA^+ cations is not known.

Here, we use synchrotron radiation ($h\nu = 53.0$ eV) to ionize FA, which thus undergoes single-photon outer-valence ionization. We investigate the further evolution of FA^+ ions populated in the electronic states lying in the 10–19 eV range, that we probe specifically using e^-–ion coincidences. For interpretation of the experimental findings, we performed post-Hartree–Fock *ab initio* computations on the structure and the fragmentation pathways of ground and electronically excited FA^+ ions, where we mapped the doublet and quartet potentials along suitable coordinates. In particular, the present data highlights the importance of vibronic couplings between the electronic states of FA^+, playing a key role in the further dynamics of FA^+ ions. In addition, we compare the present findings with the photophysics of neutral FA. The branching ratios and dissociation dynamics are found to be quite different.

II. METHODS

A. Computational details

We used post-Hartree–Fock methodologies to identify the species issued from the fragmentation of FA^+ and the accurate energetics of the corresponding dissociation limits. Thus, geometry optimizations were performed in the C_1 symmetry point group for both

neutral and ionic FA species, as well as for all possible molecular fragments resulting from the dissociation of FA^+. These optimizations were carried out using the explicitly correlated coupled-cluster method [CCSD(T)-F12 (approximation b)],[35–38] which accounts for single, double, and perturbative triple excitations. For open-shell species, the restricted version [RCCSD(T)-F12] was used. These calculations employed the aug-cc-pVTZ basis sets[39,40] together with their associated density fitting sets,[41] as implemented in the MOLPRO (version 2015) package.[42] The molecular species we computed correspond to minima in the corresponding potential energy surfaces (PESs) as ensured by computing the respective harmonic frequencies, which were all positive.

In addition, we explored the PESs of the lowest electronic states of FA^+, considering both doublet and quartet spin multiplicities, along relevant dissociation pathways. We thus describe the evolutions of the FA^+ PESs in the vicinity of and far from the Franck–Condon zone accessed by ionizing *trans*-FA, which is the unique molecular compound present in the experiment (*vide infra*). For these electronic structure computations, we used the state-averaging complete active-space self-consistent field (SA-CASSCF)[43,44] method followed by the internally contracted multi-reference configuration interaction (MRCI)[45–47] technique, as implemented in MOLPRO. These computations were done in the C_s point group, where the A′ and A″ representations were treated equally. States with identical spin multiplicity were averaged during the CASSCF procedure. Here, the atoms, were described by the aug-cc-pV5Z basis sets.[39,40] The CASSCF active space included orbitals ranging from HOMO−8 to HOMO+4, while the MRCI space was built considering all electronic configurations generated by single and double excitations from the CASSCF wavefunctions, retaining only those with CI coefficients larger than 0.05. This results in $>4.4 \times 10^7$ contracted configuration state functions (CSFs) while treating the $^2A'$ or $^4A'$ components.

We evaluated the spin–orbit couplings between the lowest electronic states of FA^+. The spin–orbit matrix elements were determined in Cartesian coordinates using the Breit–Pauli Hamiltonian.[48] The CASSCF wavefunctions served as the multielectron basis for the two-step spin–orbit coupling calculations. Here, the aug-cc-pVTZ basis sets were used to describe the atoms. The doublet and quartet states were averaged together.

B. Experiment

The experiments were performed at the PLEIADES beamline[49] of the Synchrotron SOLEIL (France), using a photoelectron/Auger electron–photoion coincidence setup (EPICEA).[50,51] The photon beam was generated by an Apple II HU 80 permanent magnet undulator and monochromatized using the modified Petersen plane grating monochromator in combination with a high-flux 600 lines per mm grating. The photon energy was calibrated according to the $Ar(2p_{3/2}^{-1} \rightarrow 4s)$ transition at 244.39 eV,[52] with overall accuracy during the experiment better than 0.2 eV. Note that the uncertainty of the photon energy calibration does not influence the binding energy calibration, which was done according to a selected line in the XPS spectrum (see below). Also, the resolution of the photon energy was much higher than that of the photoelectron analyzer in the present experiment.

EPICEA consists of a double toroidal electron analyzer (DTA)[53] and a linear time-of-flight (TOF) mass spectrometer with 3D focusing capabilities.[54,55] The 3D (spatial) focusing was not used in the present experiment; thus, the potentials of the two focusing rings and the drift tube were all set equal (ca. −880 V). The interaction region, defined by the photon/molecular beam overlap, is placed between the two grounded grids. A voltage pulse is applied to the grids to extract the photoions toward a delay-line position-sensitive ion detector (HEX75, Roentdek GmbH) placed at the end of the TOF drift tube. The field strength in the ionization region was about 13 V/mm. A pulsed field that extracts all ions is triggered by a detected photoelectron. Additionally, a pulse generator (Stanford DG645) was used to produce "virtual" triggers, which extract ions present in the interaction region without a coincident electron event, thus allowing us to analyze and subtract the false coincidences. The latter subtraction was performed using the statistical procedure proposed by Prümper and Ueda.[56] The TOF scale was transformed to the mass/charge (m/z) scale according to the TOF values of molecular parent ions O_2^+ (m/z 32) and FA^+ (m/z 46) for each acquired spectrum. PEPICO spectroscopy was performed at hν = 53 and 61 eV for comparison. In particular, special care was taken to eliminate any contribution from residual air and water.

Electrons emitted at the magic angle are focused into the DTA by a system of lenses,[57] where they are selected according to the predetermined pass energy (Ep). The detection window of the electron kinetic energies (KEs) is ca. 12% of the defined Ep. The spectral resolution, as defined by the DTA, is about 1% of the Ep. In the present experiments, we were using Ep = 50 eV for the acquisitions at the photon energies of 53 and 61 eV, defining a DTA energy resolution of about 0.5 eV. It should be noted that the DTA resolution could be additionally deteriorated due to alignment imperfections, which have been somewhat improved by dedicated image post-processing algorithms. After passing the DTA, the selected electrons are recorded by a delay-line position-sensitive detector (DLD40, Roentdek GmbH). The distance of the electron position to the center of the detector is inversely proportional to its kinetic energy. The calibration of the DTA kinetic energy scale was performed by recording the radius positions of the Ar 3s/3p photoelectrons as a function of the photon energy in small steps and by using a previously proposed empirical formula to transform the detector radius position (mm) to the electron kinetic energy (eV).[57] The calibration of the binding energy scale in the present experiment was performed according to the known vertical ionization energy (IE) of formic acid of 11.51 eV.[24] Because of the relatively low resolution of the spectrometer, we use the vertical IE rather than the adiabatic IE of 11.3246 eV.[24,25] Appearance energies were obtained using a single-Gaussian fit applied to the peaks of binding energy spectra, following the subtraction of false coincident background signals for each m/z value. The uncertainty of the peak values is simply given according to the total spectral resolution.

SIMION simulations were performed to estimate ion kinetic energy distributions (KED) from the experimentally measured mass-specific time-of-flight peaks. The simulations were performed using SIMION 8.1, with additional Julia coding, based on a previously reported dedicated SIMION geometry.[50] Briefly, thousands of ion trajectories were generated to record ion TOFs for different ion mass/charge (m/z) values, starting KEs, the inclination angles, and spatial starting positions. The generated (TOF, KEs) SIMION

matrices were then weighted by either Maxwell–Boltzmann and/or Gaussian-broadened fixed-iKE distributions and fit to the experimentally obtained TOF peaks to estimate the KED for a given ion m/z. More details and distributions are given in the supplementary material.

The FA sample, acquired from Sigma-Aldrich (purity > 95%), was further purified through several freeze-pump-thaw degassing cycles using liquid nitrogen to remove the residual gases dissolved in the product (mainly air). FA is a liquid (T_{vap} = 8.3 °C) at P = 1 bar and room temperature, with a vapor pressure (=46 mBar at 20 °C) sufficient to inject FA gas into the experimental setup chamber via an effusive jet needle (inner diameter of 0.5 mm) and obtain a good signal level. The whole gas line outside the vacuum chamber was kept at a constant temperature of about 30 °C to ensure stable pressure in the spectrometer during long (6–15 h) acquisitions. The base pressure in the EPICEA chamber was about 3×10^{-8} mbar, while the working pressure was kept in the region of $1–2 \times 10^{-7}$ mbar, which—together with the low photon beam intensity—ensures an acceptable number of false coincidences for further statistical processing.

III. RESULTS AND DISCUSSION

A. Photoelectron spectrum

FA^+ ionic states are reached from the FA ground state either after valence or inner-valence single-photon ionization using synchrotron radiation at hν = 53.0 or 61.0 eV. Upon FA single ionization, we have investigated the unimolecular decomposition processes of FA^+. It should be noted that for all the above-mentioned photon energies used at the synchrotron facility, the doubly ionized states of FA were reachable; nevertheless, such processes were filtered out owing to the electron-ion coincidences.

Upon vaporizing liquid FA, it forms *a priori* spontaneously gas-phase double-hydrogen-bonded $(HCOOH)_2$ dimers (cf. Scheme 1) in addition to monomeric FA.[58] To ensure that solely monomeric FA is present prior to photoionization, we compare our experimental spectrum obtained with the EPICEA setup at the photon energy of 53 eV (Fig. 1) to the He I photoelectron (PE) spectra of FA and of $(HCOOH)_2$ that are available in Refs. 19 and 20. Figure 1 shows that our experimental spectra are similar to that of *trans*-FA,[19] although the one from EPICEA was recorded with a much lower resolution of about 0.5 eV, whereas our spectrum differs from that of the dimer. Indeed, Kimura *et al.*[20] showed that the He I PE $(HCOOH)_2$ dimer spectrum presents more bands in the 10–21 eV energy range, some of them not coinciding with those of FA. In particular, the He I PE $(HCOOH)_2$ spectrum exhibits a broad band at ~13.9 eV, which falls in the Franck–Condon gap accessed from *trans*-FA ($\tilde{X}^1A_1$). It is, therefore, missing in our experiments. Accordingly, monomeric FA is much more present than the dimer.

FA exists in two forms: *cis* and *trans* (cf. Scheme 1), the latter being the most stable one. Very recently, we performed a close comparison of the simulated photoelectron spectra of *trans*-FA and of *cis*-FA with the experimental He I PE spectra. The simulated spectra were obtained using first-principles methodologies, where we determined the equilibrium structures and vibrational frequencies of *trans*- and *cis*-FA and of their ionic species in their electronic ground and excited states. We showed that mainly the *trans*-form is obtained in the gas phase upon evaporating liquid FA, and thus contributes to He I PE spectra.[21] Consequently, we will assume that only *trans*-FA is present in our experiments. We also mapped the PESs of the doublet cationic species along various internal coordinates. These potentials revealed the complex electronic structure of these cations due to vibronic couplings resulting in the mixing of their electronic wavefunctions.

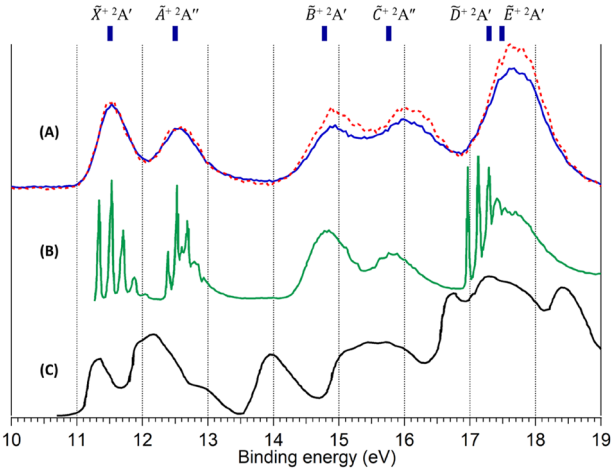

FIG. 1. In (a): Photoelectron spectrum of FA recorded with the EPICEA setup at the photon energy of 53 eV. The full blue line represents the PE obtained from all detected triggering electrons. The dashed red line represents the PE obtained as a sum of false-background-subtracted spectra for specific ion time-of-flight regions that correspond to the FA ionic fragments m/z 18, 29, 45, and 46. We also superposed the He I spectra of FA [green line, in (b)] and of $(HCOOH)_2$ [black line, in (c)] for comparison.[19,20] The vertical combs represent the vertical ionization energies of FA^+ electronic states as determined in Ref. 21. The binding energy scale is calibrated according to the FA vertical ionization energy of 11.51 eV.[24] The spectrum in (b) was reproduced with permission from Schwell *et al.*, Chem. Phys. **272**, 77 (2001). Copyright 2001 Elsevier. The spectrum in (c) was reproduced with permission from Kimura *et al.*, *Handbook of HeI Photoelectron Spectra of Fundamental Organic Molecules* (Japan Scientific Societies Press, Tokyo; Halsted Press, New York, 1981). Copyright 1981 Japan Scientific Societies Press.

B. Mass spectra

The TOF spectra of *trans*-FA ionized by 53 eV photons are presented in Fig. 2, as well as the mass spectrum obtained by TOF → mass/charge calibration. The shown spectra are obtained after the subtraction of the background due to the false coincidences, according to the statistical procedure.[56] Indeed, the photon energy of 53 eV is high enough to access the appearance thresholds of smaller fragments (see below) and is even well above the double ionization energy of FA [of ~28 eV as computed at the (R)CCSD(T)-F12/aug-cc-pVTZ level]. The formation of smaller fragments is clearly seen in the non-treated electron-triggered mass spectrum (Fig. S3). Nevertheless, the false-background subtraction dominantly preserves only the ions that are formed in coincidence with the triggering photoelectrons, corresponding to the formation of the lowest six cationic states of *trans*-FA^+ (Fig. 1). The discussion of the mass spectrum due to the residual background in the vacuum chamber is given in the supplementary material.

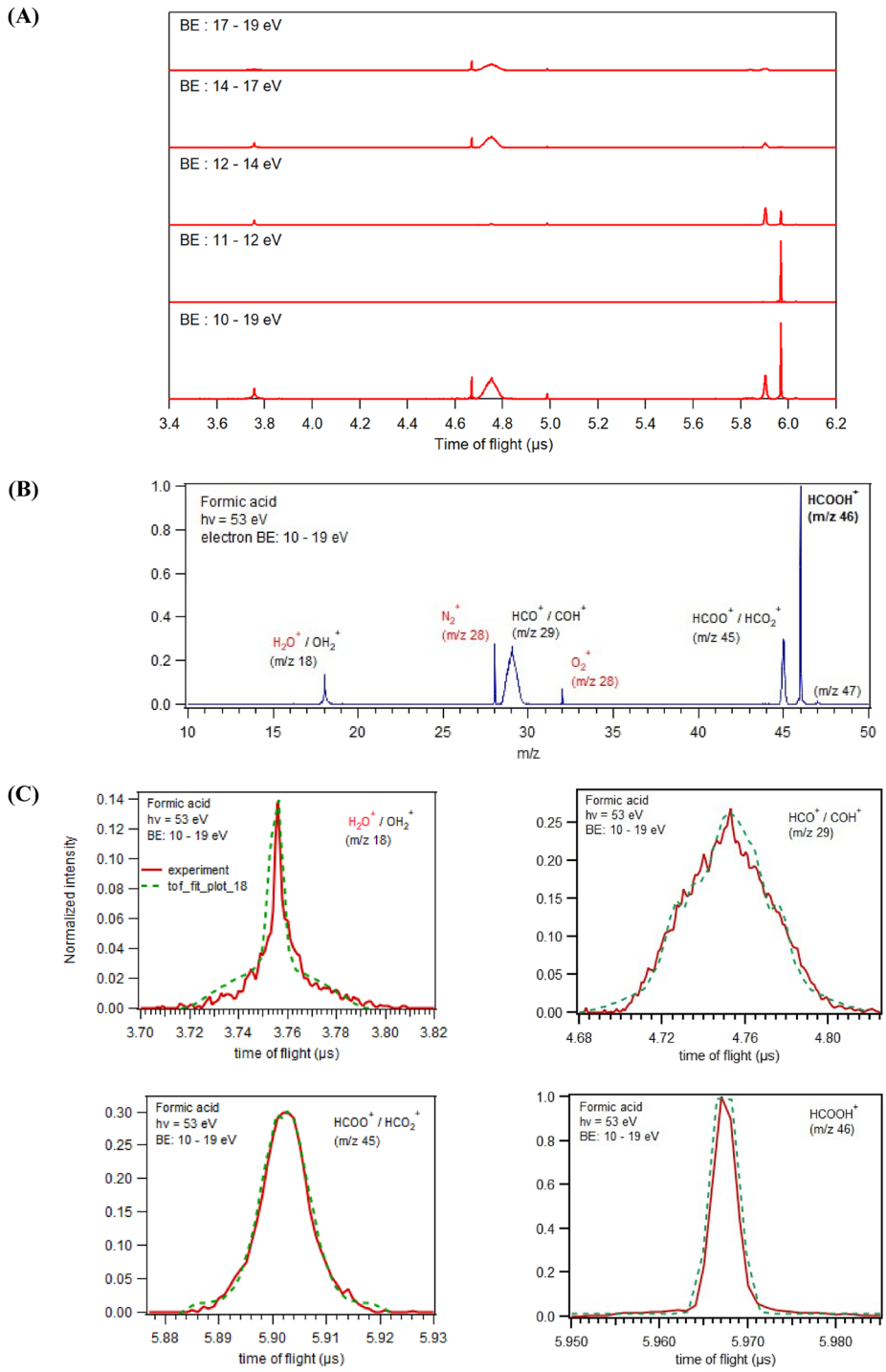

FIG. 2. (a) False-background-subtracted TOF spectra of FA fragmentation obtained at the photon energy of 53 eV, presented for different ranges of the electron binding energies. (b) False-background-subtracted mass spectrum of *trans*-FA ionized at the photon energy of 53 eV and measured in coincidence with the photoelectrons in the binding energy range of ca. 10–19 eV. The text in red color indicates the ionic fragments that correspond to the background—residual water and air (nitrogen and oxygen). (c) Selected regions in the mass spectrum that correspond to the FA fragmentation/ionization presented in TOF scale. The red line represents experimentally measured TOF spectra after false-background subtraction. The green line represents a fit to the experimental curves by simulated TOF distributions obtained from weighted combined ion kinetic energy distributions produced in SIMION simulations.

Figure 2(c) shows TOF peaks for the selected peaks in the mass spectrum that correspond to FA fragmentation/ionization. The peak that corresponds to the parent ion (m/z 46) is very narrow and has a Gaussian shape, since it is defined only by a thermal kinetic energy distribution (at ~300 K) of the target molecule. The Gaussian width of the TOF peaks for all parent ions (N_2^+, O_2^+, and FA^+) is similar (1.5–2.0 ns), showing that the thermal distribution of FA emerging from the capillary is the same as that of the residual gas in the vacuum chamber.

The simulated TOF peaks [green dashed lines in Fig. 2(c)] are obtained as the best least-square fit to the experimental curves from simulated TOF peaks produced from weighted combined ion KEDs from SIMION simulations. They provide a qualitative perspective of how the KED evolves for different ionic fragments. It is important to note that the false-background-subtracted mass spectra presented in Figs. 2(b) and 2(c) correspond to the full range of the measured binding energy range (ca. 10–19 eV). The false-subtracted coincident TOF distributions change significantly over different selected ionic states [see Fig. 2(a)].

M/z 45 corresponds to the loss of one hydrogen from the parent ion, giving either HCO_2^+ or $HOCO^+$ fragments. The TOF peak related to m/z 45 is clearly broader than the one for m/z 46 due to the recoil momentum that the fragment receives from the ejected neutral hydrogen fragment. Since the latter takes the dominant part of the momentum, the KED of m/z 45 is relatively small. The fit represents a mixture of a Gaussian broadened constant KER of ca. 0.06 eV and a statistical Maxwell–Boltzmann distribution of 0.012 eV.

The TOF peak of m/z 29, which can be attributed to the production of the HCO^+/COH^+ fragment, is very broad, suggesting a large kinetic energy released to this fragment. It has been proposed previously[23] that the formation of m/z 29 from FA^+ represents a very non-statistical process, with two KER components involved in the final KED: a small, sharp KER at about 0.1–0.3 eV, and a broad, large KED with the most probable KE close to 1 eV, at the excitation energy close to 18 eV. As mentioned above, in the present case, the KED corresponds to the whole binding energy range of ca. 10–19 eV. The green dashed line presented in Fig. 2(c) represents the best fit to the experimental TOF peaks, obtained as a mixture of two KEDs from SIMION: a small, relatively sharp KER of ~0.25 eV and a large, wide high-energy distribution with the most probable KE at ~1.0 eV, with the contribution of about 0.55 (small/total, see supplementary material for details).

As discussed in the supplementary material, m/z 18 represents an overlap of the signals that correspond to the *trans*-FA^+ fragmentation and to the ionization of the residual background water (IE = 12.6 eV[17]). Therefore, the total TOF peak of m/z 18 represents an overlap of the close to 0 eV KED corresponding to the ionization of background water, and a higher energy KED originating from the dissociation of FA^+. The fit to the experimental TOF peak presented in Fig. 2(c) is a mixture of a statistical distribution close to 0 eV and a KER of ca. 0.5 eV.

Finally, the peak at m/z 47 could, in principle, come from the $(HCOOH)_2$ dimer photoionization followed by intradimer proton transfer and then fragmentation. Still, its intensity in the background-subtracted mass spectrum is ca. 1.5% of m/z 46 (precursor), meaning that it dominantly corresponds to the ^{13}C isotope of FA ($^{13}C/^{12}C$ = 1.1%). This is an additional confirmation that the influence of the $(HCOOH)_2$ dimer is rather small/negligible in our study, as already discussed above.

By increasing the photon energy to 61 eV, we store more energy into FA^+, leading to an increased abundance of smaller FA^+ fragments (m/z 10–18), as well as m/z 45 (H-loss) with respect to m/z 46, as seen in the non-subtracted electron-triggered mass spectrum (Fig. S3, right panels). It also slightly increases the abundance of m/z 47, showing more efficient fragmentation of the $(HCOOH)_2$ dimer, which is inevitably present in small proportion here. Still, since the ion detection is triggered only by the formation of the lowest FA^+ electronic states, the false-background-subtracted spectrum at 61 eV is much like the one at 53 eV (Fig. S3, left panels), with a notable relative increase of m/z 45 and m/z 18 with respect to the parent ion m/z 46. However, it is important to note that the coincident spectrum at the photon energy of 61 eV was recorded only for up to ca. 16 eV of electron binding energy, which drastically influences the coincident mass spectrum, as mentioned above [cf. Fig. 2(a)]. Therefore, one cannot make a direct comparison. Indeed, the reduced binding energy range of up to 16 eV efficiently eliminates the contribution of m/z 28 (N_2, IE = 15.6 eV[17]).

C. PEPICO spectra

Figure 3 shows the PEPICO maps of *trans*-FA as obtained at photon energies of hν = 53 and 61 eV, in the overlapping electron binding energy region of ca. 10–16 eV. The 2D maps (related only to 1 electron–1 ion events), obtained after subtraction of the false coincidences, show the correlation between the binding energy of *trans*-FA^+ electronic states and the m/z of the cationic species formed upon ionizing *trans*-FA. It can also be seen that the false-background-subtracted coincident electron spectra locked to the lowest FA^+ ionic states are similar at both photon energies, as also shown by integrating the PEPICO spectra at selected m/z values and presenting the "horizontal slices" for each species (Fig. S5).

Figure 4 presents the binding energy spectra of *trans*-FA^+ in coincidence with selected m/z values of 46, 45, 29, and 18, respectively, where we also marked the *trans*-FA^+ electronic states lying in this binding energy range. Rather than slicing the 2D PEPICO maps, the spectra in Fig. 4 were obtained by reducing the total acquisition statistics to a selected ion TOF region, corresponding to the desired m/z value [see Fig. 2(c)], then applying the false coincidence background subtraction, which increases the statistical accuracy (see Ref. 56). Such spectra corresponding to m/z 28 and m/z 32 are presented in Fig. 6, clearly confirming a different electron binding energy distribution than for FA, and in good agreement with the previously reported electronic bands of N_2 and O_2,[20] originating in the present case from the background air. The analysis of the coincidence spectrum of m/z 18 is much more complicated. As we discussed above, the latter TOF region is an overlap of low-KE ions coming from the ionization of the background water, and the high-KE ions coming from the fragmentation of FA^+. Therefore, two coincidence binding energy spectra were generated corresponding, respectively, to the sum of high-energy TOF wings (Fig. S7A, blue line) and the central low-energy TOF region (Fig. S7B, red line). The spectrum for the low-KE TOF has much higher signal in the binding energy range 12–13 eV and practically three electronic bands that correlate well with the positions of the H_2O spectrum[20]

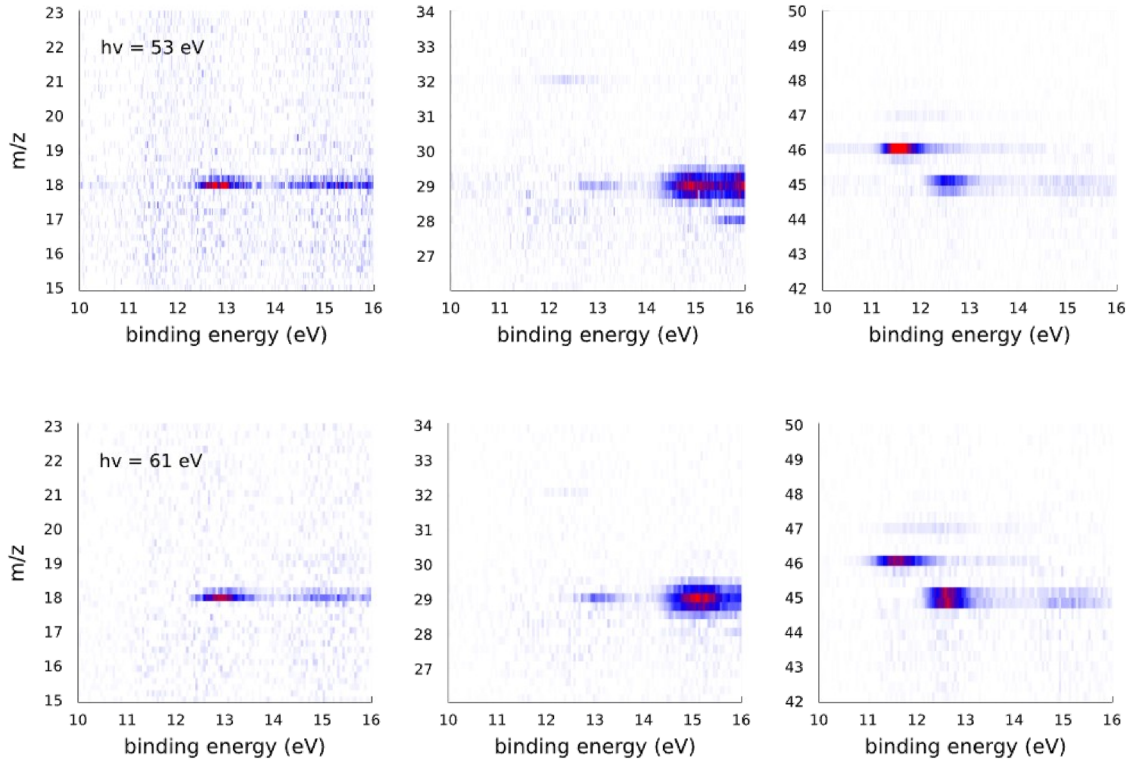

FIG. 3. False-background-subtracted PEPICO spectra of FA fragmentation obtained at the photon energy of 53 eV (top) and 61 eV (bottom).

(Fig. S7B). Therefore, although full resolving of the two contributions (background water and FA) cannot be obtained, we will consider in further analyses the spectrum at m/z 18 for high-KE TOF as corresponding to the fragmentation of FA^+.

Figure 4(a) shows the PEPICO spectrum for m/z 46. A unique band between 11 and 12 eV binding energies is observed, due to the formation of FA^+. The corresponding TOF peak in Fig. 2 is narrow as expected for such a parent ion. The shape of the band in Fig. 4(a) is not symmetric, extending toward higher binding energies. The beginning of the band agrees with the measured and computed adiabatic ionization energy of *trans*-FA (~11.33 eV[20,21]) and the maximum of this band matches the measured vertical ionization energy (of 11.51 eV[24]). According to Ref. 21, this band corresponds to the formation of stable *trans*-FA^+ ions in the $\tilde{X}^+\ ^2A'$ state and in the low-lying vibrational levels of the $\tilde{A}^+\ ^2A''$ state.

Figure 4(b) presents the PEPICO spectrum cut associated with the m/z 45 fragment. This figure reveals that the signal rises for binding energies ~12 eV. Three bands can be seen: (i) The first one (the biggest) is located between 12 and 13.5 eV, which corresponds mostly to the population of the *trans*-FA^+ ($\tilde{A}^+\ ^2A''$) state. (ii) The second band extends from 14.2 up to 16.6 eV. It is associated with the formation of *trans*-FA^+ ($\tilde{B}^+\ ^2A'$ and $\tilde{C}^+\ ^2A''$) ions. (iii) The third band ranges from 16.6 to 18.8 eV, where *trans*-FA^+ ($\tilde{D}^+\ ^2A'$ and $\tilde{E}^+\ ^2A'$) states are populated. Note that these signals may also coincide with the population of the high vibronic levels of the other electronic states lying at these energies. These bands correspond to the loss of a hydrogen atom from *trans*-FA^+, forming *a priori* either the HCO_2^+ or $HOCO^+$ isomeric fragments. The analysis of the TOF distribution of these ions [Fig. 2(c)] leads to a close-to-zero KER for these ions of 0.012/0.08 eV.

Figure 4(c) displays the PEPICO spectrum for the m/z = 29 fragment, most likely due to HCO^+ or COH^+ ions. This spectrum is composed of a weak band starting at ~12.5 eV and extending to ~13.5 eV, corresponding to the population of the *trans*-FA^+ ($\tilde{A}^+\ ^2A''$) state. Then, the spectrum continues with three intense broad bands centered at ~14.9, ~16, and ~17.8 eV, which are associated with the fragmentation of *trans*-FA^+ ($\tilde{B}^+\ ^2A'$), *trans*-FA^+ ($\tilde{C}^+\ ^2A''$) and *trans*-FA^+ ($\tilde{D}^+\ ^2A'$ and $\tilde{E}^+\ ^2A'$) ions, respectively. Figure 2(c) shows that these ions are produced with a combination of two KER components, a small one of ~0.25 eV and a wide high energy distribution with the most probable KE at ~1.0 eV, and with the ratio 0.56 (small/large). The determination of two KERs associated with this fragment is consistent with previous observations. Indeed, Niwa *et al.*[22] deduced KERs of ~0.9 and <0.3 eV for this fragment using TPEPICO. This bimodal KER distribution was confirmed later by Nishimura *et al.*[23]

Figure 4(d) shows the PEPICO spectrum for m/z 18 corresponding to higher KE ions (see Fig. S7A). This spectrum is composed of four bands with maxima at ~12.6, ~15, ~16, and ~17.5 eV, which correspond to the population, prior to fragmentation, of the *trans*-FA^+ ($\tilde{A}^+\ ^2A''$), *trans*-FA^+ ($\tilde{B}^+\ ^2A'$), *trans*-FA^+ ($\tilde{C}^+\ ^2A''$), and *trans*-FA^+ ($\tilde{D}^+\ ^2A'$ and $\tilde{E}^+\ ^2A'$) states, respectively.

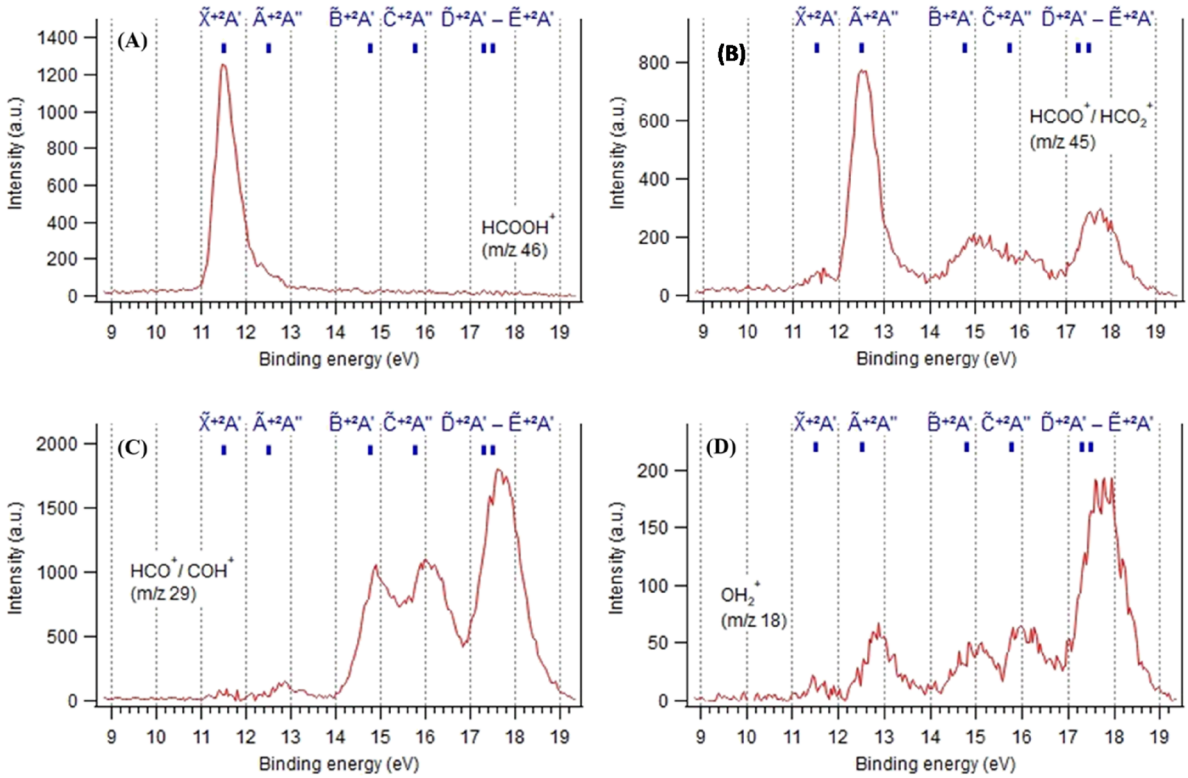

FIG. 4. PEPICO spectra obtained at the photon energy of 53 eV, presenting the binding energy spectra for FA^+ (m/z 46, TOF: 5.963–5.972 μs) in (a), $HCOO^+/HCO_2^+$ (m/z 45, TOF: 5.87–5.93 μs) in (b), HCO^+/COH^+ (m/z 29, TOF: 4.68–4.83 μs) in (c), and H_2O^+ (m/z 18, TOF: 3.7–3.752 + 3.76–3.8 μs) in (d). The vertical bars represent the vertical ionization energies of *trans*-FA^+ electronic states.[21]

D. Appearance energies

Figure 5 shows the energy diagram of $HCOOH^+$ species, including *trans*-FA^+, $HOCOH^+$, and H_2OCO^+ isomers and their fragments located in the 11–19 eV energy range and relevant for the present study. These data are computed at the (R)CCSD(T)-F12/aug-cc-pVTZ level. In addition, we positioned the TS1 transition state connecting *trans*-FA^+ and $HOCOH^+$. $HOCOH^+$, H_2OCO^+, and TS1 were previously found at the SD-CI/6-31G**//UHF/4-31G[33] and MP3/6-31G*//HF4-31G[34] levels. At the (R)CCSD(T)-F12/aug-cc-pVTZ level, $HOCOH^+$ and H_2OCO^+ are located at 10.903 and 11.655 eV with respect to *trans*-FA ($\tilde{X}\ ^1A'$). For *trans*-FA^+, we also locate the adiabatic ionization energies of its $\tilde{X}^+\ ^2A'$, $\tilde{A}^+\ ^2A''$, $\tilde{B}^+\ ^2A'$, $\tilde{C}^+\ ^2A''$, $\tilde{D}^+\ ^2A'$, and $\tilde{E}^+\ ^2A'$ states.[21]

At the (R)CCSD(T)-F12/aug-cc-pVTZ level, the lowest asymptote, $HOCO^+$ ($\tilde{X}^+\ ^1A'$) + H (^2S), is calculated at 12.63 eV (Table I). The formation of the HCO_2^+ isomer by H loss from *trans*-FA^+ [i.e., HCO_2^+ ($\tilde{X}^+\ ^1A_1$) + H (^2S) asymptote] is computed at 16.96 eV. The HCO^+ ($\tilde{X}^+\ ^1\Sigma^+$) + OH ($\tilde{X}\ ^2\Pi$) dissociation limit is located at 13.05 eV (Table I), whereas the COH^+ ($\tilde{X}^+\ ^1\Sigma^+$) + OH ($\tilde{X}\ ^2\Pi$) asymptote is calculated 1.72 eV higher in energy (at 14.77 eV) in agreement with the HCO^+–COH^+ known relative energies (of 1.7 eV[61]). The H_2O^+ ($\tilde{X}^+\ ^2B_1$) + CO ($\tilde{X}\ ^1\Sigma^+$) and H_2O ($\tilde{X}\ ^1A_1$) + CO^+ ($\tilde{X}^+\ ^2\Sigma^+$) asymptotes are found at 13.06 and 14.40 eV, respectively. For energies >18 eV, we may have the deprotonation of FA^+, producing *cis*- and *trans*-HOCO for energies >18.17 and 18.24 eV, respectively, and the $OH^+(X^+\ ^3\Sigma^-)$ ions formation [+HCO ($\tilde{X}\ ^2A'$)] for energies >18.02 eV. In addition, we give in Fig. 5 the asymptotes located in the 11–19 eV energy domain and associated with the electronically excited species listed in this paragraph.

Using the PEPICO spectra of Fig. 4, we estimated the appearance energies (AEs) of m/z 45, 29, and 18 species. They are listed in Table I together with those measured previously. We also give those computed presently at the (R)CCSD(T)-F12/aug-cc-pVTZ level and at the DFT–B3LYP/6-311++G(3df,3pd) level by Arruda *et al.*[29] The latter are 0.1–0.4 eV lower than ours, since DFT underestimates such quantities, as discussed in Refs. 66–69, (R)CCSD(T)-F12/aug-cc-pVTZ AEs should be viewed as more accurate. While comparing our experimental AEs to previously measured ones, one can see that we are closer to the accurate *ab initio* data. The assignment of molecular structures is based on the present theoretical findings (see below). In addition, the m/z 18 signal may come either from residual water or the fragmentation of *trans*-FA^+ ions. Note that the determined AE of this fragment by Nishimura *et al.*[23] and by Arruda *et al.*[29] (of 12.6 eV) is distinctly lower than the computed values (of 12.91 and 13.06 eV), whereas their value is

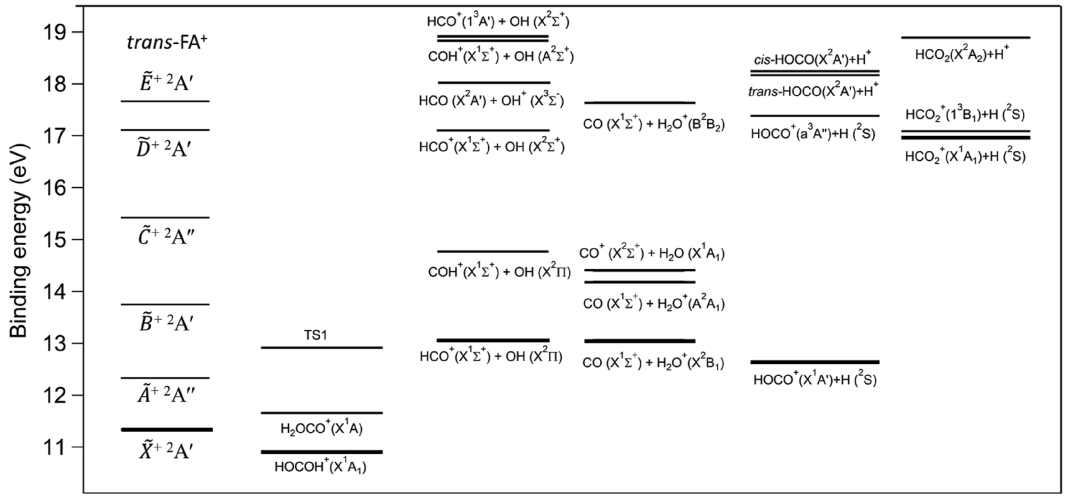

FIG. 5. Energy diagram showcasing the adiabatic ionization energies of *trans*-FA^+ in its six lowest doublet electronic excited states as determined in Ref. 21. We also give the energies of the dissociation channels lying in the 10–19 eV energy range as computed at the (R)CCSD(T)-F12/aug-cc-pVTZ level of theory. The total energies and geometrical parameters of the fragments are compiled in Tables S1–S4. The electronic excitation energies of OH, OH^+, HCO, CO, and CO^+ have been taken from the NIST database,[17] of HCO^+ from Ref. 59, and of H_2O^+ from Ref. 60. TS1 is the transition state connecting *trans*-FA^+ and $HOCOH^+$ (cf. Ref. 34). The thick lines correspond to the molecular species in their respective electronic ground state. The structures of the molecular species are given in Scheme 2.

TABLE I. Appearance energies (in eV) of *trans*-FA^+ fragmentation channels. See text.

		Theory		Experiment						
m/z	Channel	This work[a]	Reference 29 [b]	This work[c]	Reference 29 [d]	Reference 62 [e]	Reference 63 [f]	Reference 64 [g]	Reference 65	Reference 23 [h]
45	$HCO_2^+ + H$	16.96	16.35	17.71 ± 0.25						
45	$HOCO^+ + H$	12.63	12.26	12.55 ± 0.25	12.24	12.1 ± 0.1	12.36			12.21 ± 0.14
29	$HCO^+ + OH$	13.05	12.60	12.88 ± 0.25	12.62	12.8 ± 0.2		12.79		12.62 ± 0.11
29	$COH^+ + OH$	14.77	14.42	14.95 ± 0.25 16.07 ± 0.25 17.69 ± 0.25					14.21	
18	$H_2O^+ + CO$	13.06	12.91	12.88 ± 0.25 15.03 ± 0.25 16.07 ± 0.25	12.46	13.1 ± 0.1				12.62 ± 0.11

[a](R)CCSD(T)-F12/aug-cc-pVTZ values as given in thick lines in Fig. 5.
[b]DFT – B3LYP/6-311++G(3df,3pd).
[c]PEPICO.
[d]TOF-mass spectrometry.
[e]Electron impact.
[f]Photoionization mass spectrometry.
[g]Photoionization mass spectrometry.
[h]TPEPICO.

close to the ionization energy of water (of ~12.6 eV[17]) as confirmed by the detection, in those experiments, of m/z 17 signal at 19.4/18.17 eV due to dissociative photoionization of water. Such a signal is absent in the present experiments. In fact, we have also some—but minor—contamination by residual water [cf. Fig. 4(d)]. After examination of Fig. 4(d), we can state safely that the m/z 18 signal >14 eV binding energy is due to the fragmentation of *trans*-FA^+ ions. In particular, the band expanding between 17 and 18 eV does not correspond to any electronic state of H_2O^+. However, it correlates well with the $\tilde{D}^+ {}^2A'$ and $\tilde{E}^+ {}^2A'$ states of *trans*-FA^+.

Table I shows that two AEs are associated with m/z 45, namely 17.71 and 12.55 eV. The former AE is equal to the one we deduce for the highest AE of m/z 29. We also determine close AEs for m/z 29 and m/z 18 of ~12.9, ~15, and ~16.1 eV. In fact, fragment ions having the same AE are issued from the further evolution of the same FA^+ intermediate state.

E. State-to-state fragmentation of *trans*-FA$^+$

In this section, we describe the unimolecular decomposition of each HCOOH$^+$ electronic state. The comparison of the computed and the measured AEs suggests that we have *a priori* the formation of HCO$^+$/COH$^+$, H_2O^+, and HOCO$^+$/HCO_2^+ fragments upon state-selective dissociative photoionization of *trans*-FA. Although HCO$^+$ and HOCO$^+$/HCO_2^+ fragments may result from simple bond breaking, the formation of COH$^+$ and H_2O^+ requires intramolecular arrangements and may involve the HOCOH$^+$ and H_2OCO^+ isomers. These reactions may occur in the ground and electronic excited states PESs of *trans*-FA$^+$ as displayed in Figs. 6–8.

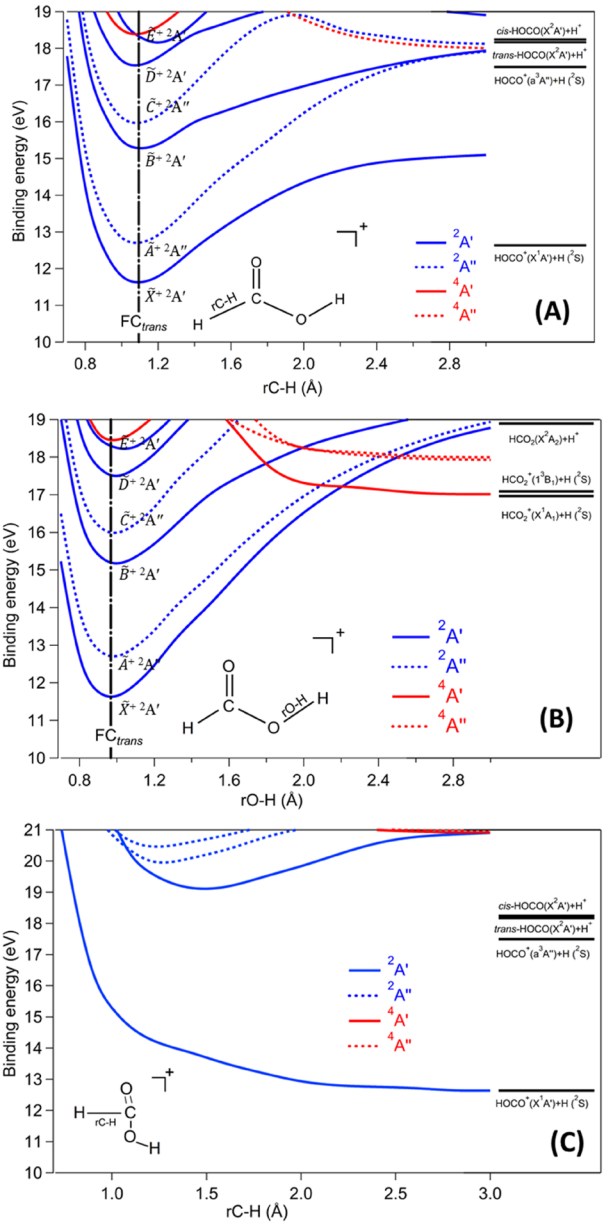

FIG. 6. MRCI/aug-cc-pV5Z 1D cuts of the PESs of the lowest electronic states of *trans*-FA$^+$. These cuts are done along the C–H distance [in (a) and (c)] and along the O–H distance in (b). The remaining coordinates were kept fixed at their equilibrium values in *trans*-FA ($\tilde{X}\,^1$A′) [in (a) and (b)] while in (c) the geometry used is the equilibrium structure of the HOCO$^+$ ($\tilde{X}^+\,^1$A′) fragment. FC$_{trans}$ corresponds to the middle of the Franck–Condon region accessed from *trans*-FA ($\tilde{X}\,^1$A′). The reference energy is that of *trans*-FA ($\tilde{X}\,^1$A′) at equilibrium.

1. m/z 45

The formation of the m/z 45 fragment is due to the loss of a hydrogen atom from *trans*-FA$^+$. Table I shows that two ions may be associated with this TOF peak: HOCO$^+$ with an AE of 12.55 ± 0.25 eV or HCO_2^+ with an AE of 17.71 ± 0.25 eV after the breaking of the CH or the OH bonds. For both, a close-to-zero KER is measured. As can be seen in Scheme 2, the formation of HOCO$^+$ is accompanied by large structural modifications, in particular, the OCO in-plane angle, which evolves from ~125° in *trans*-FA$^+$ to ~175° in HOCO$^+$. For those purposes, we mapped the PESs of *trans*-FA$^+$ in the Franck–Condon region accessed from *trans*-FA along the CH and OH bonds [Figs. 6(a) and 6(b)], while relaxing the OCO angle from 120° to 180° (Fig. S6) and close to the HCO + OH asymptote [Fig. 6(c)]. These potential cuts should help in shedding light on the hydrogen loss from *trans*-FA$^+$.

For binding energies <17 eV, Fig. 5 shows that solely HOCO$^+$ ($\tilde{X}^+\,^1$A′) + H (^{2}S) fragments are obtained. These fragments have *trans*-FA$^+$ ($\tilde{X}^+\,^2$A′, $\tilde{A}^+\,^2$A″, $\tilde{B}^+\,^2$A′ and $\tilde{C}^+\,^2$A″) states as parents since they are located in this energy range (Fig. 1). The most intense peak in the respective PEPICO spectrum [Fig. 4(b)] is associated with the high vibrational levels of *trans*-FA$^+$ ($\tilde{X}^+\,^2$A′) and of *trans*-FA$^+$ ($\tilde{A}^+\,^2$A″). As discussed in Ref. 21, the $\tilde{B}^+\,^2$A′ and $\tilde{C}^+\,^2$A″ states are coupled vibronically and evolve to populate the $\tilde{A}^+\,^2$A″ state via internal conversion. The $\tilde{A}^+\,^2$A″ state is in turn coupled vibronically with the $\tilde{X}^+\,^2$A′ state. The conical intersection between the $\tilde{X}^+\,^2$A′ and $\tilde{A}^+\,^2$A″ states occurs for rC–O of ~1.7 Å (Fig. S6A). The shortening of the rC–O distance to 1.2 Å, as in isolated HOCO$^+$ ($\tilde{X}^+\,^1$A′) (Fig. S6B), allows relaxing the long-range parts of the potentials to converge to the HOCO$^+$ ($\tilde{X}^+\,^1$A′) + H (^{2}S) asymptote. Then, the reaction evolves along the ground potential [Fig. 6(c)], where the HOCO$^+$ ions are produced with close to zero KER, in good agreement with the present experimentally determined KER.

For binding energies >17 eV, the situation is quite complicated because of the opening of several (*cis*-/*trans*-)HOCO$^{0/+}$ + H$^{+/0}$ and $HCO_2^{0/+}$ + H$^{+/0}$ channels (Fig. 5) and because of the high density of doublet electronic states of *trans*-FA$^+$ at these energies that are populated upon single-photon ionizing *trans*-FA. In addition, Fig. 6 shows that the quartet states are lying at these energies and may participate in the unimolecular decomposition processes. The dynamics of *trans*-FA$^+$ ions at these energies is complex: Fig. 6(a) shows that we first populate the $\tilde{D}^+\,^2$A′ state either directly from *trans*-FA or after $\tilde{E}^+\,^2$A′ - $\tilde{D}^+\,^2$A′ internal conversion starting from the $\tilde{E}^+\,^2$A′ state of *trans*-FA$^+$, since both states are vibronically coupled.[21] *trans*-FA$^+$ ($\tilde{D}^+\,^2$A′) ions may convert to the lower electronic states leading to deprotonation or H-loss channels in connection with HOCO$^{0/+}$ species. Alternatively, Fig. 6(b) reveals that the ($\tilde{X}^+\,^2$A′, $\tilde{A}^+\,^2$A″, $\tilde{B}^+\,^2$A′ and $\tilde{C}^+\,^2$A″) potentials along the OH distance are crossed by the quartet potentials at these energies, where spin–orbit conversion may take place. These crossings are at 18.81, 17.84, 17.25, and 17.22 eV energies [i.e., at 1.61, 1.79, 2.09, and 2.21

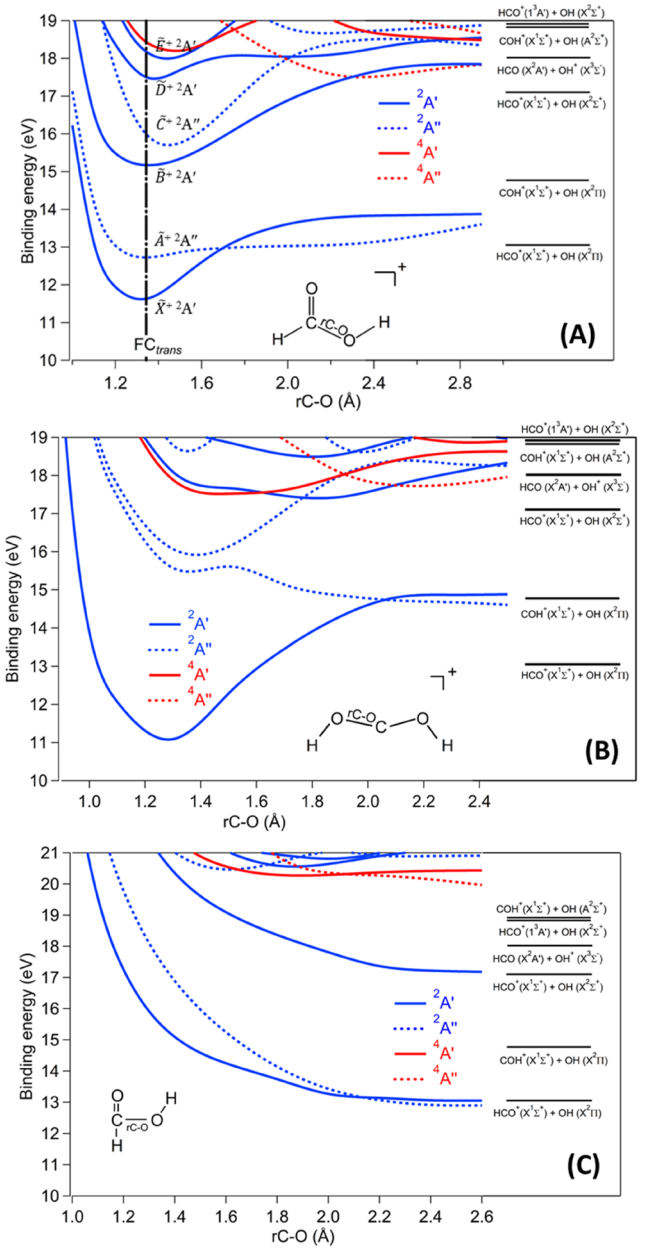

FIG. 7. MRCI/aug-cc-pV5Z 1D cuts of the potential energy surfaces of *trans*-FA^+ [in (a) and (c)] and of $HOCOH^+$ [in (b)] electronic states lying in the 10–21 eV binding energy range. These cuts are done along the rC–O distance, where remaining coordinates are set to their values at equilibrium in *trans*-FA^+ ($\tilde{X}^+ {}^2A'$) [in (a)], or in $HOCOH^+$ ($\tilde{X}^+ {}^2A_1$) [in (b)], or in HCO^+ ($\tilde{X}^+ {}^1\Sigma^+$) and OH ($\tilde{X}\,{}^2\Pi$) [in (c)]. cf. Tables S1–S4 for more details. The reference energy is that of *trans*-FA ($\tilde{X}\,{}^1A'$) at equilibrium.

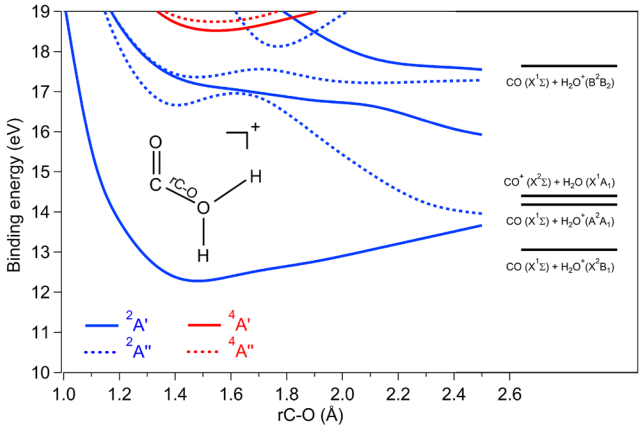

FIG. 8. MRCI/aug-cc-pV5Z 1D cuts of the PESs of H_2OCO^+ electronic states along the central CO (rC–O) distance. The remaining coordinates are kept fixed at their equilibrium values in H_2OCO^+ electronic ground state (Tables S1–S4). The reference energy is that of *trans*-FA ($\tilde{X}\,{}^1A'$) at equilibrium.

(in Å) rO–H distances] for the $\tilde{C}^+ {}^2A'' - 1\,{}^4A'$, $\tilde{B}^+ {}^2A' - 1^4A'$, $\tilde{A}^+ {}^2A'' - 1^4A'$ and $\tilde{X}^+ {}^2A' - 1^4A'$ crossings, respectively. In addition, the corresponding spin–orbit integrals are evaluated to be non-zero (cf. Tables S5–S7), allowing such conversion. The quartets correlate to the HCO_2^+ + H channels directly and without a barrier. Accordingly, KERs of a few tenths of eV are predicted, in agreement with the <0.1 eV experimentally determined ones. Specifically, we believe that $\tilde{X}^+ {}^2A' - 1^4A'$ is the most efficient pathway since we do measure close-to-zero KER for the HCO_2^+ ions.

2. m/z 29

The AEs determined after the analysis of the PEPICO spectrum associated with m/z 29 of 12.88 ± 0.25 eV and 14.95 ± 0.25 eV (Table I) are associated with the formation of the HCO^+ + OH or COH^+ + OH fragments. The former (latter) carry a KER of ~0.25 eV (~1 eV). Although the formation of HCO^+ from *trans*-FA^+ can be explained by obvious central C–O bond breaking, that of its isomer COH^+ *a priori* occurs after intramolecular isomerization followed by C–O breaking. To shed light on these processes, we present in Fig. 7 the one-dimensional evolution of the potentials of *trans*-FA^+ and of its isomer $HOCOH^+$ along the C–O distance, where their remaining coordinates are kept fixed at their values at equilibrium (Tables S1–S4).

For binding energies <14 eV, the production of HCO^+ coincides with the population of the *trans*-FA^+ ($\tilde{A}^+ {}^2A''$) state [Fig. 4(c)], which correlates adiabatically to the HCO^+ ($X^1\Sigma^+$) + OH($X^2\Pi$). Nevertheless, Fig. 7(a) shows that its potential is quite high in the FC$_{trans}$ region, which could result in HCO^+ ions produced with very large KER. This is not confirmed by the present and previous experimental observations. Instead, this figure shows that the energy position of the HCO^+ ($X^1\Sigma^+$) + OH($X^2\Pi$) asymptote coincides with the crossing between the *trans*-FA^+ ($\tilde{X}^+ {}^2A'$ and $\tilde{A}^+ {}^2A''$) states (i.e., their conical intersection). The vibronic coupling between both states is efficient allowing to convert *trans*-FA^+ ($\tilde{A}^+ {}^2A''$) into *trans*-FA^+ ($\tilde{X}^+ {}^2A'$) ions,[21] which lead to the desired products after HCO and OH internal coordinates relaxation [cf. Fig. 7(c)]. Therefore, the HCO^+ ions are produced with small KER values as measured experimentally. In addition, this confirms that the experimentally observed broadening of the vibronic bands of the

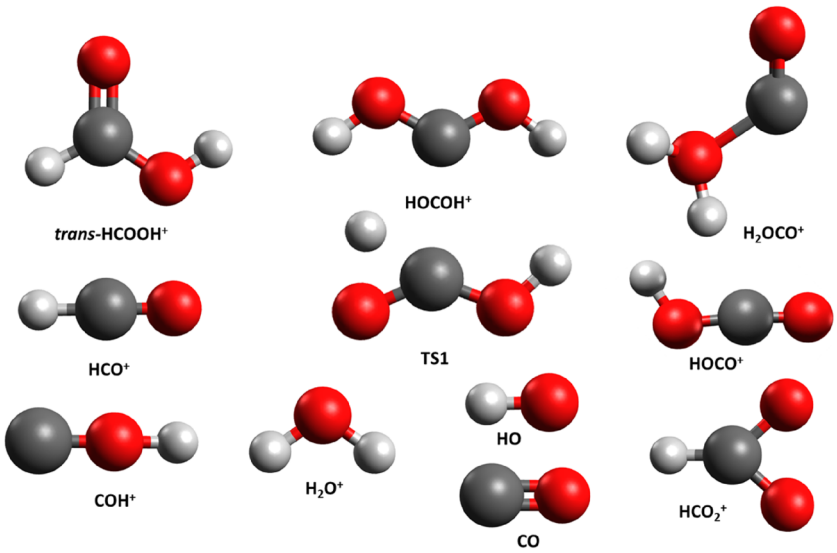

SCHEME 2. Structures of the molecular species given in Fig. 5.

trans-FA^+ ($\tilde{A}^+\,^2A''$) state is due to their predissociation to the HCO^+ ($X^1\Sigma^+$) + $OH(X^2\Pi)$ limit.[21]

For binding energies >14 eV, the PEPICO spectrum of m/z 29 is composed of intense broad bands associated with the production of these ions after population of the *trans*-FA^+ ($\tilde{B}^+\,^2A'$, $\tilde{C}^+\,^2A''$, $\tilde{D}^+\,^2A'$, and $\tilde{E}^+\,^2A'$) states. Such enhancement of band intensities is a signature of more efficient processes compared to low binding energies. However, Fig. 7(a) shows that these electronic states do not correlate adiabatically to the lowest HCO^+ + OH asymptote and correlate to the excited dissociation limits (located >17 eV). Also, the *trans*-FA^+ ($\tilde{B}^+\,^2A'$) → *trans*-FA^+ ($\tilde{A}^+\,^2A'$) internal conversion is not favored since the corresponding vibronic coupling is zero.[21] They hence cannot produce efficiently HCO^+ ions in the 13–17 eV energy domain. In contrast, the $COH^+(X^1\Sigma^+)$ + $OH(X^2\Pi)$ limit is lying at 14.773 eV. At these energies, the m/z 29 ions correspond, therefore, to COH^+ (in majority) and not to HCO^+. For explanation, we propose first a *trans*-FA^+ → $HOCOH^+$ isomerization, which takes place along the potentials of the *trans*-FA^+ ($\tilde{B}^+\,^2A'$, $\tilde{C}^+\,^2A''$, $\tilde{D}^+\,^2A'$, and $\tilde{E}^+\,^2A'$) excited states. Such an intramolecular process is possible since we are above the lowest transition state (TS1, Fig. 5) connecting both species. The electronic states of $HOCOH^+$ are populated, in particular, the two lowest $^2A''$ states. Figure 7(b) reveals that the lowest $^2A''$ state possesses a local minimum at ~15.48 eV separated from the $COH^+(X^1\Sigma^+)$ + $OH(X^2\Pi)$ by a small potential barrier (of ~0.14 eV). The fragmentation from this state leads to COH^+ with a computed KER of ~0.85 eV, close to the ~1 eV KER value estimated experimentally. In addition, the congestion in *trans*-FA^+ ($\tilde{B}^+\,^2A'$, $\tilde{C}^+\,^2A''$) photoelectron bands is due to their enlargement by predissociation leading to $COH^+(X^1\Sigma^+)$ + $OH(X^2\Pi)$.

3. m/z 18

As for the previously discussed COH^+ ions, the direct production of H_2O^+ ions upon single-photon ionizing *trans*-FA is not possible. Obviously, a 1,3-proton transfer from the C of the formyl group to the O of the hydroxyl group should occur first, resulting in the formation of the H_2OCO^+ ions. Such a process takes place through three-step reactions involving two transition states before reaching H_2OCO^+ as discussed by Uggerud *et al.*[34] Nevertheless, these authors showed that this mechanism goes through a step that requires too much energy (276 kJ/mol = 2.86 eV), which is not consistent with the measured AE of the H_2O^+ fragment. For remediation, Ruttink and Burgers[33] proposed an alternative mechanism where the OH roams around the HC=O moiety via the conical intersection between the $\tilde{X}^+\,^2A'$ and $\tilde{A}^+\,^2A''$ states of *trans*-FA^+ (Fig. S6). A $(HCO\cdots OH)^+$ ion/dipole complex is formed, which evolves to the H_2OCO^+ isomer without needing to overcome a too-high energy barrier (of 1.33–1.47 kJ/mol, i.e., 0.013–0.015 eV). Afterward, the H_2O^+ + CO fragments can be obtained via central CO bond breaking in H_2OCO^+. These unimolecular processes evolve along the potentials of the electronic states of the H_2OCO^+ isomer, as depicted in Fig. 8. Figure 4(d) shows that the water ions are produced after population of *trans*-FA^+ electronic states located >14 eV. Such ions evolve to populate the lowest potential of H_2OCO^+ after internal conversion. Then, this potential leads directly to the desired products with small KERs, consistent with the KER of ~0.5 eV we determine for m/z 18 ions originating from *trans*-FA^+. In sum, this mechanism supports the appearance of CO + H_2O^+ fragments close to the observed threshold.[23]

IV. CONCLUSIONS

Using a combined PEPICO and post-Hartree–Fock *ab initio* computations, we investigated the mechanisms undergone by *trans*-FA^+ formed upon single-photon ionization of the corresponding neutral species. The major channels are confirmed to be the proton ejection and the central C–O bond breaking either before or after intramolecular isomerization processes via the $HOCOH^+$ or H_2OCO^+ isomers. In particular, we showed that the state-to-state decomposition of *trans*-FA^+ ions produces HCO^+ or COH^+ and $HOCO^+$ or HCO_2^+ isomeric forms depending on the initially populated parent cationic electronic state. We showed also

the importance of vibronic and spin–orbit couplings during these processes. In addition, we proved that H_2O^+ formation is a minor channel although CO and H_2O are major fragments issued from the photodissociation of neutral *trans*-FA, which also leads efficiently to CO_2 + H_2.[70] Presently, we have no clear evidence of the production of CO_2^+ ions from *trans*-FA^+. Note that CO_2^+ was detected after multiphoton ionization of a mixture of *cis*- and *trans*-FA.[32] Accordingly, *cis*-FA^+ might produce CO_2^+. We highly suggest investigating the state-to-state *cis*-FA^+ unimolecular decomposition, as done presently, to confirm such a conformational memory effect as established for the neutral species.[71]

In an astrophysical context, the present mechanisms should be incorporated into the astrochemical models to better model the further evolution of FA after photoionization and its contribution to the formation of the astrophysical ions HCO^+/COH^+ and $HOCO^+$. In addition, HCO_2^+, an isomer of $HOCO^+$, is not detected yet. We, however, identified an efficient pathway for its formation upon decomposing *trans*-FA^+ with hν > 17 eV. Our work suggests strongly searching for this ion in the ISM.

SUPPLEMENTARY MATERIAL

See the supplementary material for detailed description of the SIMION simulations, the treatment of the false coincidences, and the deduction of the experimental KEs and AEs discussed in the manuscript. We also give the computed geometrical parameters of the molecular species considered presently, the potentials, and the spin–orbit coupling terms needed for the discussion of the fragmentation pathways.

ACKNOWLEDGMENTS

Experiments were carried out at the PLEIADES beamline of the SOLEIL storage ring (Saint Aubin, France), proposal ID 20231852. We thank the SOLEIL staff for technical assistance and the stable operation of the equipment and storage ring during the experiments. We thank Dr. Christophe Nicolas (Synchrotron SOLEIL, France) for help during experiments.

AUTHOR DECLARATIONS

Conflict of Interest

The authors have no conflicts to disclose.

Author Contributions

A. Gloriod: Data curation (equal); Formal analysis (equal); Investigation (equal); Writing – original draft (equal); Writing – review & editing (equal). **A. R. Milosavljević**: Conceptualization (equal); Data curation (equal); Formal analysis (equal); Investigation (equal); Methodology (equal); Resources (equal); Software (equal); Validation (equal); Visualization (equal); Writing – original draft (equal); Writing – review & editing (equal). **A. Bellili**: Data curation (equal); Investigation (equal); Writing – review & editing (equal). **J. Palaudoux**: Data curation (equal); Investigation (equal); Methodology (equal); Resources (equal); Validation (equal); Writing – review & editing (equal). **F. Penent**: Data curation (equal); Investigation (equal); Validation (equal); Writing – review & editing (equal). **R. Dupuy**: Data curation (equal); Validation (equal); Writing – review & editing (equal). **M. Hochlaf**: Conceptualization (equal); Data curation (equal); Formal analysis (equal); Funding acquisition (equal); Investigation (equal); Methodology (equal); Project administration (equal); Resources (equal); Software (equal); Supervision (equal); Validation (equal); Visualization (equal); Writing – original draft (equal); Writing – review & editing (equal).

DATA AVAILABILITY

The datasets supporting this article have been uploaded as part of the supplementary material.

REFERENCES

[1] J. S. Francisco, J. T. Muckerman, and H.-G. Yu, "HOCO radical chemistry," Acc. Chem. Res. **43**, 1519 (2010).
[2] P. A. S. Randi, D. F. Pastega, M. H. F. Bettega, N. C. Jones, S. V. Hoffmann, S. Eden, A. Souza Barbosa, and P. Limão-Vieira, Spectrochim. Acta, Part A **289**, 122237 (2023).
[3] C. Huang, C. Zhang, and X. Yang, J. Chem. Phys. **132**, 154306 (2010).
[4] S. Maeda, T. Taketsugu, K. Ohno, and K. Morokuma, J. Am. Chem. Soc. **137**, 3433 (2015).
[5] L. Khriachtchev, E. Maçôas, M. Pettersson, and M. Räsänen, J. Am. Chem. Soc. **124**, 10994 (2002).
[6] B. Zuckerman, J. A. Ball, and C. A. Gottlieb, Astrophys. J. **163**, L41 (1971).
[7] G. Winnewisser and E. Churchwell, Astrophys. J. **200**, L33–L36 (1975).
[8] S. Cuadrado, J. R. Goicoechea, O. Roncero, A. Aguado, B. Tercero, and J. Cernicharo, Astron. Astrophys. **596**, L1 (2016).
[9] V. Taquet, E. S. Wirström, A. Charnley, A. Faure, A. López-Sepulcre, and C. M. Persson, Astron. Astrophys. **607**, A20 (2017).
[10] M. Agúndez, N. Marcelino, J. Cernicharo, E. Roueff, and M. Tafalla, Astron. Astrophys. **625**, A147 (2019).
[11] P. Thaddeus, M. Guélin, and R. A. Linke, Astrophys. J. **246**, L41 (1981).
[12] M. Bogey, C. Demuynck, and J. L. Destombes, Astron. Astrophys. **138**, L11 (1984).
[13] D. Buhl and L. E. Snyder, Nature **228**, 267 (1970).
[14] R. C. Woods, T. A. Dixon, R. J. Saykally, and P. G. Szanto, Phys. Rev. Lett. **35**, 1269 (1975).
[15] E. Herbst and W. Klemperer, Astrophys. J. **185**, 505 (1973).
[16] H. M. Boechat-Roberty, S. Pilling, and A. C. F. Santos, Astron. Astrophys. **438**, 915 (2005).
[17] See https://webbook.nist.gov for the ionization energies of some molecular species considered in the present work.
[18] S. Bell, T. L. Ng, and A. D. Walsh, J. Chem. Soc., Faraday Trans. 2 **71**, 393 (1975).
[19] M. Schwell, S. Leach, K. Hottmann, H.-W. Jochims, and H. Baumgärtel, Chem. Phys. **272**, 77 (2001).
[20] K. Kimura, S. Katsumata, Y. Achiba, T. Yamazaki, and S. Iwata, *Handbook of HeI Photoelectron Spectra of Fundamental Organic Molecules* (Japan Scientific Societies Press, Tokyo; Halsted Press, New York, 1981).
[21] A. Gloriod, M. Mogren Al-Mogren, and M. Hochlaf, Phys. Chem. Chem. Phys. **27**, 25483 (2025).
[22] Y. Niwa, T. Nishimura, F. Isogai, and T. Tsuchiya, Chem. Phys. Lett. **74**, 40 (1980).
[23] T. Nishimura, G. G. Meisels, and Y. Niwa, J. Chem. Phys. **91**, 4009 (1989).
[24] S. Leach, M. Schwell, F. Dulieu, J.-L. Chotin, H.-W. Jochims, and H. Baumgärtel, Phys. Chem. Chem. Phys. **4**, 5025 (2002).

[25]M. Schwell, F. Dulieu, H.-W. Jochims, J.-H. Fillion, J.-L. Lemaire, H. Baumgärtel, and S. Leach, J. Phys. Chem. A **106**, 10908 (2002).
[26]T. Tepnual, L. Feketeová, V. Grill, P. Scheier, Z. Herman, and T. D. Märk, Int. J. Mass Spectrom. **244**, 164 (2005).
[27]S. Pilling, A. C. F. Santos, W. Wolff, M. M. Sant'Anna, A. L. F. Barros, G. G. B. De Souza, N. V. De Castro Faria, and H. M. Boechat-Roberty, Mon. Not. R. Astron. Soc. **372**, 1379 (2006).
[28]M. R. F. Siggel-King, A. J. Yencha, G. C. King, A. E. R. Malins, and M. Eypper, J. Electron Spectrosc. Relat. Phenom. **185**, 204 (2012).
[29]M. S. Arruda, R. R. T. Marinho, A. M. Maniero, M. S. P. Mundin, A. Mocellin, S. Pilling, A. N. de Brito, and F. V. Prudente, J. Phys. Chem. A **116**, 6693 (2012).
[30]M. M. Fujimoto, H. K. Tanaka, R. R. T. Marinho, A. Medina, F. V. Prudente, and M. G. P. Homem, J. Phys. Chem. A **124**, 6478 (2020).
[31]C. Stråhlman, A. Kivimäki, R. Richter, and R. Sankari, Phys. Rev. A **96**, 023409 (2017).
[32]C. Cisneros, T. Bautista, C. F. Betancourt, E. Prieto, A. Guerrero, and I. Álvarez, J. Nucl. Phys., Mater. Sci., Radiat. Appl. **8**, 197 (2021).
[33]P. J. A. Ruttink and P. C. Burgers, Int. J. Mass Spectrom. Ion Processes **113**, 23 (1992).
[34]E. Uggerud, W. Koch, and H. Schwarz, Int. J. Mass Spectrom. Ion Processes **73**, 187 (1986).
[35]T. B. Adler, H. J. Werner, and F. R. Manby, J. Chem. Phys. **130**, 054106 (2009).
[36]T. B. Adler and H. J. Werner, J. Chem. Phys. **130**, 241101 (2009).
[37]T. B. Adler, G. Knizia, and H.-J. Werner, J. Chem. Phys. **127**, 221106 (2007).
[38]G. Knizia, T. B. Adler, and H. -J. Werner, J. Chem. Phys. **130**, 054104 (2009).
[39]T. H. Dunning, J. Chem. Phys. **90**, 1007 (1998).
[40]R. A. Kendall, T. H. Dunning, and R. J. Harrison, J. Chem. Phys. **96**, 6796 (1992).
[41]K. E. Yousaf and K. A. Peterson, J. Chem. Phys. **129**, 184108 (2008).
[42]H.-J. Werner, P. J. Knowles *et al.*, *MOLPRO, ab initio programs package*, 2015, see http://www.molpro.net.
[43]P. J. Knowles and H.-J. Werner, Chem. Phys. Lett. **115**, 259 (1985).
[44]H.-J. Werner and P. J. Knowles, J. Chem. Phys. **82**, 5053 (1985).
[45]H.-J. Werner and P. J. Knowles, J. Chem. Phys. **89**, 5803 (1998).
[46]P. J. Knowles and H.-J. Werner, Chem. Phys. Lett. **145**, 514 (1988).
[47]K. R. Shamasundar, G. Knizia, and H.-J. Werner, J. Chem. Phys. **135**, 054101 (2011).
[48]A. Berning, M. Schweizer, H.-J. Werner, P. J. Knowles, and P. Palmieri, Mol. Phys. **98**, 1823 (2000).
[49]See https://www.synchrotron-soleil.fr/en/beamlines/pleiades for an extensive presentation of the PLEIAIDES beamline including its technical specifications, experimental setups, beamline news, and publications.
[50]X.-J. Liu, C. Nicolas, M. Patanen, and C. Miron, Sci. Rep. **7**, 2898 (2017).
[51]S. Ganguly, M. Gisselbrecht, P. Eng-Johnsson, R. Feifel, P.-A. Hervieux, Z. Alfaytarouni, R. F. Fink, S. Díaz-Tendero, A. R. Milosavljević, P. Rousseau, and S. Maclot, Phys. Chem. Chem. Phys. **24**, 28994 (2022).
[52]C. Nicolas and C. Miron, J. Electron Spectrosc. Relat. Phenom. **185**, 267 (2012).
[53]C. Miron, M. Simon, N. Leclercq, and P. Morin, Rev. Sci. Instrum. **68**, 3728 (1997).
[54]D. P. Seccombe and T. J. Reddish, Rev. Sci. Instrum. **72**, 1330 (2001).
[55]R. Wu *et al.*, Meas. Sci. Technol. **34**, 055502 (2023).
[56]G. Prümper and K. Ueda, Nucl. Instrum. Methods Phys. Res., Sect. A **574**, 350 (2007).
[57]X.-J. Liu, C. Nicolas, and C. Miron, Rev. Sci. Instrum. **84**, 033105 (2013).
[58]J. Karle and L. O. Brockway, J. Am. Chem. Soc. **66**(4), 574 (1944).
[59]B. Weis and K. Yamashita, J. Chem. Phys. **99**, 9512 (1993).
[60]S. Y. Truong *et al.*, Chem. Phys. **355**, 183 (2009).
[61]A. J. Chalk and L. Radom, J. Am. Chem. Soc. **119**(32), 7573 (1997).
[62]T. Mariner and W. Bleakney, Phys. Rev. **72**, 792 (1947).
[63]M. E. Akopyan and Y. Villem, High Energy Chem. **10**, 24 (1976).
[64]P. Warneck, Z. Naturforsch. A **29**, 350 (1974).
[65]S. G. Lias, J. E. Bartmess, J. F. Liebmann, J. L. Holmes, R. D. Levin, and W. G. Mallard, J. Phys. Chem. Ref. Data **17**, 1 (1998).
[66]H. R. Hrodmarsson, M. Schwell, N. Fray, J.-C. Guillemin, M. Hochlaf, and E.-L. Zins, Astrophys. J. **964**, 26 (2024).
[67]J. Bourgalais, H.-H. Carstensen, O. Herbinet, G. A. Garcia, P. Arnoux, L.-S. Tran, G. Vanhove, L. Nahon, M. Hochlaf, and F. Battin-Leclerc, J. Phys. Chem. A **126**(34), 5784 (2022).
[68]J. Bourgalais, O. Herbinet, H.-H. Carstensen, J. Debleza, G. A. Garcia, P. Arnoux, L.-S. Tran, G. Vanhove, B. Liu, Z. Wang, M. Hochlaf, L. Nahon, and F. Battin-Leclerc, Energy Fuels **35**, 19689 (2021).
[69]I. Derbali, H. R. Hrodmarsson, Z. Gouid, M. Schwell, M.-C. Gazeau, J.-C. Guillemin, M. Hochlaf, M. E. Alikhani, and E.-L. Zins, Phys. Chem. Chem. Phys. **21**, 14053 (2019).
[70]Y.-S. Ku and P.-Y. Tsai, J. Phys. Chem. A **129**, 1068 (2025).
[71]C.-J. Tso, T. Kasai, and K.-C. Lin, Sci. Rep. **10**, 4769 (2020).